

# Driving up the Electrocatalytic Performance for Carbon Dioxide Conversion through Interface Tuning in Graphene Oxide–Bismuth Oxide Nanocomposites

Michele Melchionna,\* Miriam Moro, Simone Adorinni, Lucia Nasi, Sara Colussi, Lorenzo Poggini, Silvia Marchesan, Giovanni Valenti,\* Francesco Paolucci, Maurizio Prato, and Paolo Fornasiero\*



Cite This: *ACS Appl. Energy Mater.* 2022, 5, 13356–13366



Read Online

ACCESS |



Metrics & More



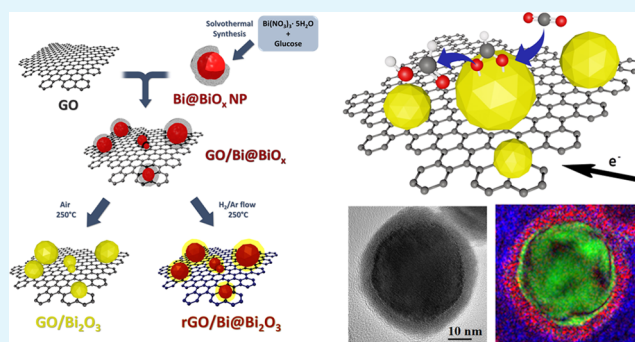
Article Recommendations



Supporting Information

**ABSTRACT:** The integration of graphene oxide (GO) into nanostructured  $\text{Bi}_2\text{O}_3$  electrocatalysts for  $\text{CO}_2$  reduction ( $\text{CO}_2\text{RR}$ ) brings up remarkable improvements in terms of performance toward formic acid ( $\text{HCOOH}$ ) production. The GO scaffold is able to facilitate electron transfers toward the active  $\text{Bi}_2\text{O}_3$  phase, amending for the high metal oxide (MO) intrinsic electric resistance, resulting in activation of the  $\text{CO}_2$  with smaller overpotential. Herein, the structure of the GO–MO nanocomposite is tailored according to two synthetic protocols, giving rise to two different nanostructures, one featuring reduced GO (rGO) supporting  $\text{Bi}@\text{Bi}_2\text{O}_3$  core–shell nanoparticles (NP) and the other GO supporting fully oxidized  $\text{Bi}_2\text{O}_3$  NP. The two structures differentiate in terms of electrocatalytic behavior, suggesting the importance of constructing a suitable interface between the nanocarbon and the MO, as well as between MO and metal.

**KEYWORDS:** graphene oxide, bismuth oxide, carbon dioxide reduction, electrocatalysis, interfaces



## INTRODUCTION

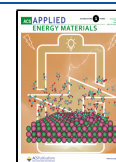
A switch to sustainable energy and chemical production is in urgent demand, triggering a vast amount of research toward the implementation of new schemes with low environmental impacts. In this context, the electrochemical reduction of carbon dioxide ( $\text{CO}_2\text{RR}$ ) into value-added products is a highly desirable strategy to create a closed carbon cycle for fuels and chemicals.<sup>1,2</sup> The  $\text{CO}_2\text{RR}$  can proceed with a variety of possible products, including the thermodynamically more favored  $\text{H}_2$  evolution (HER) when the reaction is carried out in aqueous electrolytes.<sup>3–5</sup> This aspect is the main driving force for the continuous development of new selective and active  $\text{CO}_2\text{RR}$  electrocatalysts able to operate in aqueous environment. Bismuth-based heterogeneous catalysts have flourished in recent years as attractive  $\text{CO}_2\text{RR}$  electrocatalysts, leading mainly to the formation of formic acid ( $\text{HCOOH}$ ), a very useful feedstock for the chemical and fuel cell industry.<sup>6,7</sup> Most studies focused on metallic  $\text{Bi}(0)$ , whose typical selectivity toward  $\text{HCOOH}$ <sup>8–12</sup> arises from the favorable adsorption of the  $^*\text{OCHO}$  intermediate onto the Bi surface in comparison with  $^*\text{COOH}$  and  $^*\text{H}$ .<sup>10,12</sup> Nevertheless, downsides are identified with the usually large required overpotentials and modest current densities,<sup>9,13–15</sup> as well as short operation time stability.<sup>16,17</sup> These shortcomings inspired the search for engineered Bi-based catalyst structures, in order to

achieve  $\text{CO}_2\text{RR}$  at small overpotential with competitive intrinsic activity and selectivity. During our exploration of electrocatalytic  $\text{CO}_2\text{RR}$ , we have provided evidence on how the integration of carbon nanostructures (CNS) into carbon/metal oxide (MO) nanocomposite can harness a cascade of events that enables the catalytically active site to be active at earlier onset potentials with increased selectivity toward  $\text{HCOOH}$ .<sup>18,19</sup> This synergistic effect arises from the formation of suitable carbon–inorganic interfaces, whereby the CNS is able to (1) improve charge transfers at the interface with the metal/metal oxide, (2) add up to the catalyst's stability, and (3) facilitate reactant diffusion to the active site, typically by increasing the available surface area and favoring the adsorption capacity of  $\text{CO}_2$ .<sup>20,21</sup> Herein, we chose to explore graphene oxide (GO) as the nanocarbon phase because of its large two-dimensional (2D) morphology, which allows optimum deposition of the MO nanoparticles with no size limitations, and also to focus on the electronic effects, ruling

Received: June 28, 2022

Accepted: October 11, 2022

Published: October 20, 2022



out contributions from the high surface area that could arise with higher surface area CNS such as carbon nanohorns (CNH) or carbon nanotubes (CNT). The use of conductive carbon matrices has been proven to be a proficient strategy to improve current densities of  $\text{Bi}_2\text{O}_3$  electrocatalysts, although selectivity toward  $\text{HCOOH}$  remained limited to large applied overpotentials,<sup>22</sup> so that additional complexity must be considered in  $\text{Bi}_2\text{O}_3$ -based hybrid catalyst design. Recent reported studies illustrated the role of oxidation of Bi to  $\text{Bi}_2\text{O}_3$  and how this causes a more pronounced  $\text{CO}_2$  adsorption and a quicker first electron transfer step to form the initial  $\text{CO}_2^-$  radical intermediate, leading to enhanced catalytic performances.<sup>23</sup> Hence, we explore the synergistic combination of GO and  $\text{Bi}_2\text{O}_3$  toward improved  $\text{CO}_2\text{RR}$ , with activity boosted by the competent electron mediating role of the CNS, which allows faster kinetics.

The GO/ $\text{Bi}_2\text{O}_3$  nanocomposite, assembled by exploiting the GO oxygenated functional groups for better binding of the MO phase, exhibits different  $\text{CO}_2\text{RR}$  catalytic behavior depending on the specific structural evolution during the synthetic protocol. The observed electrocatalytic behavior in relation to the nanocomposite structure allows one to uncover many of the subtle shades that strongly affect the complex dynamics of  $\text{CO}_2\text{RR}$  driven by carbon–MO interfaces. In particular, we analyzed the correlation of the  $\text{CO}_2\text{RR}$  performance when the inorganic nanoparticles (NP) evolve from a  $\text{Bi@BiO}_x$  core–shell configuration featuring an amorphous  $\text{BiO}_x$  shell to (i) a fully oxidized and partially crystalline  $\beta\text{-Bi}_2\text{O}_3$  NPs interfaced with GO or (ii) a truly  $\text{Bi@}\beta\text{-Bi}_2\text{O}_3$  core–shell NP interfaced with reduced GO (rGO) obtained via a reductive thermal treatment. The obtained  $\text{CO}_2\text{RR}$  correlation indicates significant differences, and will help to establish a platform for the rational design of future and advanced multiphase  $\text{CO}_2\text{RR}$  electrocatalysts integrating CNS.

## ■ EXPERIMENTAL SECTION

**Synthesis of GO–Bismuth Oxide Nanocomposites.** The GO was prepared following a procedure we previously adopted.<sup>24</sup> First, 200 mg of pristine graphene was added into a 100 mL round-bottomed flask containing  $\text{K}_2\text{S}_2\text{O}_8$  (200 mg, 0.37 mmol),  $\text{P}_2\text{O}_5$  (100 mg, 0.35 mmol), and  $\text{H}_2\text{SO}_4$  (10 mL). The reaction was sonicated for 30 min and stirred at 80 °C for 4 h. The crude was cooled down, diluted with deionized water (50 mL), filtered through a Millipore membrane (JHWP, 0.45  $\mu\text{m}$ ), and washed with deionized water until neutralization of the washings. The black powder collected from the Millipore membrane was transferred into a round-bottom flask and dispersed in 20 mL of  $\text{H}_2\text{SO}_4$  at 0 °C. Then, 100 mg of  $\text{KMnO}_4$  (0.63 mmol) were added into the dispersion under stirring. The final was stirred at 35 °C for 2 h. After that, deionized water (20 mL) and  $\text{H}_2\text{O}_2$  30% (2.4 mL) were added, and the reaction was stirred for 15 min. The crude was filtered through a Millipore membrane (JHWP, 0.45  $\mu\text{m}$ ) and washed with HCl 1 M (100 mL) and deionized water until neutralization of the washings occurred. Finally, the black powder was washed one time with MeOH and dried with  $\text{Et}_2\text{O}$ , affording 210 mg of GO.

**$\text{Bi@BiO}_x$  NP.** The pristine core–shell nanoparticles were prepared via a solvothermal method adapting a reported procedure.<sup>25</sup>  $\text{Bi}(\text{NO}_3)_3 \cdot 5\text{H}_2\text{O}$  and glucose in molar ratio (1:1.5) were dissolved in ethylene glycol so to have a concentration of 0.067 and 0.1 M, respectively. The solution was stirred for 30 min and then transferred to a Teflon-lined stainless autoclave, and it was heated to 120 °C for 12 h. The black solid was recovered by centrifugation and washed successively with  $\text{H}_2\text{O}$  and ethanol.

**$\text{Bi@Bi}_2\text{O}_3$  NP.** The as prepared  $\text{Bi@BiO}_x$  NP samples were subjected to calcination at 250 °C under static air atmosphere, with a ramp of 3 °C  $\text{min}^{-1}$ .

**GO/ $\text{Bi@BiO}_x$ .** GO and  $\text{Bi@BiO}_x$  NP were prepared in different weight ratios (3:1, 4:1, 5:1). The procedure involved the dispersion under sonication of the two solids in ethanol so to have approximately a 2:1 mg  $\text{mL}^{-1}$  dispersion of GO. After the sonication, the mixture was stirred at room temperature for 24 h. The solid was recovered by centrifugation.

**GO/ $\text{Bi}_2\text{O}_3$ .** The as prepared GO/ $\text{Bi@BiO}_x$  samples were subjected to calcination at 250 °C under static air atmosphere, with a ramp of 3 °C  $\text{min}^{-1}$ .

**rGO/ $\text{Bi@Bi}_2\text{O}_3$ .** The as prepared GO/ $\text{Bi@BiO}_x$  samples were subjected to thermal treatment at 250 °C in a tubular furnace under a flowing stream of a mixture of  $\text{H}_2/\text{Ar}$  (230 mL  $\text{min}^{-1}$ , with 30 mL of  $\text{H}_2$  and 200 mL of Ar).

**Materials Physical Characterization.** Raman spectra were recorded with an Invia Renishaw microspectrometer equipped with He–Ne laser at 532 nm (1% power). At least 10 spectra per sample in different spots were collected to check their homogeneity. X-ray diffraction (XRD) was performed on a Philips X'Pert diffractometer using a monochromatized  $\text{Cu K}\alpha$  ( $\lambda = 0.154$  nm) X-ray source in the range  $10^\circ < 2\theta < 100$ . X-ray photoelectron spectroscopic (XPS) analyses were performed in an UHV chamber with a base pressure lower than  $10^{-9}/10^{-10}$  mbar. The chamber was equipped with nonmonochromatized Al radiation ( $h\nu = 1486.6$  eV) and a hemispherical electron/ion energy analyzer (VSW mounting a 16-channel detector). The operating power of the X-ray source was 1440 W (12 kV and 12 mA) and photoelectrons were collected normal to the sample surface, maintaining the analyzer angle between analyzer axis and X-ray source fixed at  $54.5^\circ$ . All the samples were adsorbed on aluminum foil, and XPS spectra were acquired in a fixed analyzer transmission mode with a pass energy of 44.0 eV. The spectra were analyzed by using the CasaXPS software. Shirley functions have been used to subtract the background. The deconvolution of the XPS spectra has been carried out employing a Lorentzian asymmetric, and the binding energies (B.E.) were calibrated upon fixing the Al 2p component of Al(0) at 71.8 eV. Transmission electron microscopy (TEM) was performed using a JEOL 2200FS microscope working at 200 kV equipped with an energy dispersive X-ray spectrometer (EDX), a high-angle annular dark-field (HAADF) detector, and an in-column energy Omega filter. EDX maps were obtained in scanning TEM (STEM) mode.

**Electrochemical Characterization.** The electrochemical characterization was performed with a SP-300 bipotentiostat (*Biologic Instruments*) workstation, using a three-electrode system composed of a saturated calomel electrode (SCE) as the reference electrode, a Pt wire as the counter electrode, and a catalyst-modified glassy carbon electrode (GCE, 3 mm in diameter, geometric surface area 0.071  $\text{cm}^2$ ) as the working electrode. The electrochemical characterization was realized in Ar-saturated KOH 0.1 M electrolyte.

To study the electrochemical properties of  $\text{Bi}_2\text{O}_3$  composites materials, a thin film was deposited on glassy carbon electrode through drop-casting. For this work, a constant loading of electrocatalyst was used, equal to 505  $\mu\text{g cm}^{-2}$ . To deposit the materials, it was necessary to disperse them in suitable solvent: the GO/ $\text{Bi}_2\text{O}_3$  were dispersed in ink of two parts of Milli-Q water and one part of 2-propanol and 0.5% Nafion with a concentration of 1.6 mg  $\text{mL}^{-1}$ . For all electrochemical measurements, the potentials were reported versus RHE and corrected for ohmic drop. The quantity of electrocatalyst deposited and the electrochemical activity comparison were made by normalizing by the Bi oxide amount of each electrocatalyst, which was measured by thermogravimetric analysis (TGA) (Figure S8).

**$\text{CO}_2\text{RR}$  Characterization.** A SP-150 potentiostat (*Biologic Instruments*) workstation and a custom-made electrochemical cell<sup>1</sup> with three-electrode configuration were used to determine the properties of  $\text{Bi}_2\text{O}_3$  composites for the  $\text{CO}_2$  reduction reaction ( $\text{CO}_2\text{RR}$ ). The innovation of this custom-made cell is the WE placed face-up in the bottom of cell, and the CE (mesh Pt) separated from the electrolyte by porous frit. With this configuration, the gas products can go directly toward the gas chromatograph (GC) for detection, and due to the separate compartment, the liquid products of  $\text{CO}_2\text{RR}$

cannot react with CE. An Ag/AgCl was used as a reference electrode (LowProfile 3.5 mm OD of PINE research). The peculiarity of this electrode is the use of a gel instead of a KCl solution. The gel and the ceramic porous frit guarantee a low mobility of the chloride ions, preventing them from escaping from the electrode with consequent poisoning of the catalyst.

The electrolyses were performed in a near-neutral bicarbonate buffer,  $\text{KHCO}_3$  0.5 M. This electrolyte was pre-electrolyzed before use to guarantee high purity, as it is known that even small amounts of metal impurities can lead to surface interference with electrochemical reactions. Pre-electrolysis was carried out in a cell with a two-electrodes configuration, with Pt wire as a counter electrode and a Pt mesh as a working electrode; electrolysis of the electrolyte was performed for at least 24 h at a current of 0.1 mA while stirring the solution, which was Ar-saturated.<sup>2</sup>

As for electrochemical characterization, the same inks and loading of materials were used for the  $\text{CO}_2$ RR study, but in this case, a bigger electrode area was used (GCE, geometric surface area  $1 \text{ cm}^2$ ). The electrode area is important because the larger the electrode area, the higher the concentration of the reaction products. In this way the detection limit of the instrument (GC) is exceeded, guaranteeing the reliability and reproducibility of the measurements.

The  $\text{CO}_2$ RR activity was evaluated by chronoamperometry (CA) of 1 h and 51 min in  $\text{CO}_2$ -saturated electrolytes. The gaseous products were analyzed during measurements by online gas chromatography (GC) directly connecting the headspace of the electrochemical cell to the sample loop of a GC, while formic acid was detected by analysis of the liquid phase by ionic chromatography (IC) at the end of electrolysis. The gas phase quantification was carried out during the electrolysis with sampling every 15 min. The Faradaic efficiency (FE) for the gas products of  $\text{CO}_2$ RR was quantified following the procedure previously described by Baltrusaitis et al.<sup>3</sup> (eq 1)

$$\text{FE}(\%) = \frac{nF\phi F_m}{I} \quad (1)$$

where  $n$  is the number of electrons needed for  $\text{CO}_2$ RR;  $F$  is the Faraday constant;  $\phi$  is the volume fraction of the gas;  $I$  is the current, and  $F_m$  is the molar  $\text{CO}_2$  gas flow rate.

While the analyses of the liquid products were performed by means of a Metrohm model 850 Professional IC Ion Chromatograph equipped with a Metrosep A Supp 4-250/4.0 anion column and a conductivity detector. The eluent used was 0.5 mM  $\text{H}_2\text{SO}_4$ , with 15% acetone. The Faradaic efficiency (FE) for the formic acid products was quantified in the following way (eq 2):

$$\text{FE} = \frac{Q(\text{HCOO}^-)}{Q_{\text{TOT}}} \times 100 \quad (2)$$

## RESULTS AND DISCUSSION

**Synthesis and Characterization of GO–Bismuth Oxide Nanocomposites.** The  $\text{Bi@BiO}_x$  NP samples were synthesized via a facile solvothermal method in the presence of glucose as the additional reducing and stabilizing agent.<sup>25</sup> The as obtained  $\text{Bi@BiO}_x$  NP samples were then deposited onto GO in an ethanol dispersion, whereby the presence of  $\text{BiO}_x$ -adsorbed glucose favors the coupling with the GO surface. The formation of the nanocomposite ( $\text{GO/Bi@BiO}_x$ ) is confirmed by transmission electron microscopy (TEM) investigation, which shows that the  $\text{Bi@BiO}_x$  NP samples are well dispersed onto the GO (Figure S1). After separation, the solid was divided into two fractions, which were independently subjected to two different thermal treatments to cause  $\text{BiO}_x$  crystallization and removal of organic groups. One treatment consisted in a calcination under static in air at  $250 \text{ }^\circ\text{C}$  ( $\text{GO/Bi}_2\text{O}_3$ ), while in the other, the  $\text{GO/Bi@BiO}_x$  fresh sample, the thermal treatment was performed under a dynamic atmosphere

of  $\text{H}_2/\text{Ar}$  ( $\text{rGO/Bi@Bi}_2\text{O}_3$ ). Figure 1 shows a sketch of the synthesis to the two final nanocomposites.

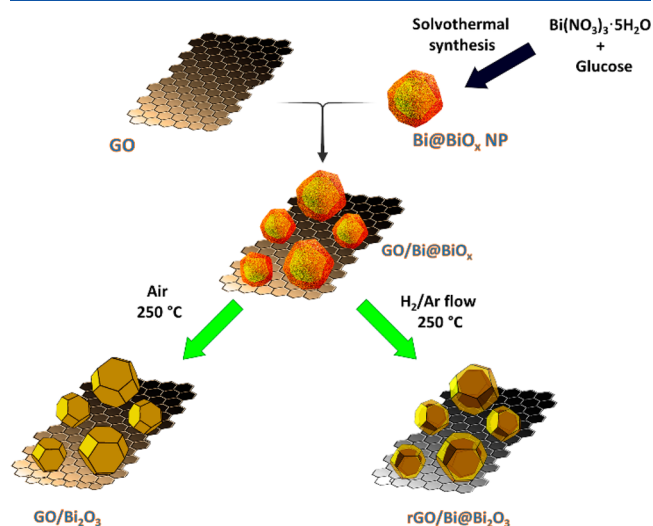


**Figure 1.** Graphical sketch of the synthesis to obtain the different nanocomposites.

The evolution of the nanocomposite structures was inspected by high resolution TEM (HRTEM), revealing the core–shell configuration of the inorganic component prior and after combination with GO. In particular, in both  $\text{Bi@BiO}_x$  and  $\text{GO/Bi@BiO}_x$ , the inorganic core consists of rhombohedral metallic Bi, identified by the interplanar  $d$ -spacing of 0.32 nm, typical of the  $\text{Bi}(012)$  plane (Figure 2a),<sup>26</sup> while the shell is made of amorphous  $\text{BiO}_x$  (Figure 2 and Figure S2). Interestingly, both the core and shell present a hexagonal geometry (Figure 2a, Figure 3d, and Figure S2). Energy dispersive X-ray analysis (EDX) provides the element mapping of C, O and Bi, and also confirms the core–shell nature of the nanoparticles, deductible from the EDX line profile spectra (Figure 2a, Figure 2b and Figure S3). The calcination treatment causes a full oxidation of the  $\text{Bi}(0)$  core to bismuth oxide, with partial formation of the metastable  $\beta\text{-Bi}_2\text{O}_3$ , as indicated by the fast Fourier transform (FFT) analysis, as well as by EDX mapping and line profile (Figure 3b). This is also noted by analyzing the HRTEM of a sample made of self-standing  $\text{Bi}_2\text{O}_3$  NP prepared by calcination of the as-prepared  $\text{Bi@BiO}_x$  without supporting them on GO (Figure S4). It is noteworthy that, despite the fact that the entire Bi is oxidized to  $\text{Bi}_2\text{O}_3$ , the morphology as observed with the TEM retains the memory of the core–shell motif, although in this case both the core and the shell are made of Bi oxide. In contrast, when the treatment is performed in  $\text{H}_2/\text{Ar}$ , the metallic Bi character of the core is preserved, while the shell becomes oxidized to  $\beta\text{-Bi}_2\text{O}_3$ ; thus, a truly  $\text{Bi@}\beta\text{-Bi}_2\text{O}_3$  core–shell structure is established, as also confirmed by the FFT analysis of the core and the shell (Figure 2c). Annular dark-field scanning transmission electron microscopy (HAADF-STEM) analysis provides neater evidence of the core–shell configuration (Figure 2c). It must be noted that in all samples the Bi oxide nanospheres are also surrounded by smaller and thinner fragments of GO, difficult to see with TEM. Nevertheless, accurate HRTEM could reveal such a structural figure, as shown in Figure S5. Moreover, different EDX color contrast on

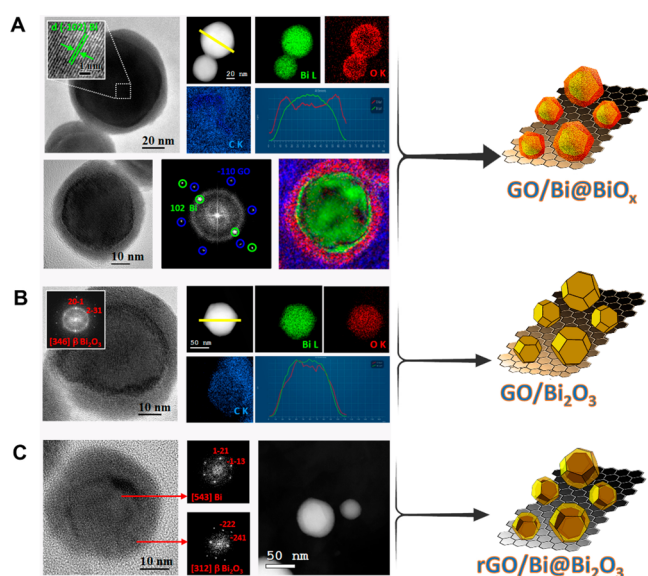


**Figure 2.** Electron microscopy study of the nanocomposites with graphical sketch of the three nanostructures. (A) Top panels from left to right: representative HRTEM image of GO/Bi@BiO<sub>x</sub> with the inset showing the *d*-spacing (−102) of Bi, HAADF-STEM image with the corresponding C, Bi, and O EDX maps. The EDX line-scan profile across the yellow line evidences the core–shell structure of Bi@Bi<sub>2</sub>O<sub>3</sub>. Bottom panels from left to right: HRTEM of GO/Bi@BiO<sub>x</sub> with corresponding FFT showing the reflections from the (−102) planes of Bi and the [001] zone axis of GO, and the diffuse ring of the amorphous shell, and a color map displaying the inverse FFT generated by selecting the reflections relative to the Bi core (green), the oxide shell (red), and the GO layer (blue). (B) Large panel: HRTEM of GO/Bi<sub>2</sub>O<sub>3</sub>. Inset: FFT of the core showing the [346] zone axis of β-Bi<sub>2</sub>O<sub>3</sub>. Small panels clockwise: HAADF-STEM image of GO/Bi<sub>2</sub>O<sub>3</sub>, with the corresponding C, Bi, and O EDX maps, and EDX line-scan profile across the yellow line. (C) Main panel: HRTEM of rGO/Bi@Bi<sub>2</sub>O<sub>3</sub> showing the crystalline core/shell structure. Small panels: FFTs of the core and the shell showing the Bi and β-Bi<sub>2</sub>O<sub>3</sub> phases respectively. Last panel: representative HAADF-STEM image.

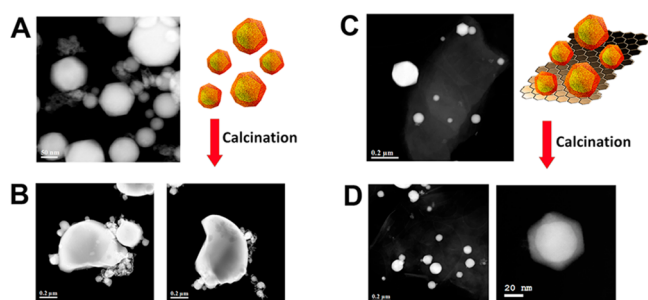


**Figure 3.** HAADF-STEM images: (A) free-standing Bi@BiO<sub>x</sub> NP, (B) free-standing Bi@BiO<sub>x</sub> after calcination at 250 °C (sample Bi<sub>2</sub>O<sub>3</sub> NP), (C) as prepared GO/Bi@BiO<sub>x</sub>, and (D) GO/Bi<sub>2</sub>O<sub>3</sub>.

the GO/Bi<sub>2</sub>O<sub>3</sub> nanocomposite shows that carbon surrounds the whole Bi<sub>2</sub>O<sub>3</sub> NPs (Figure S6).

Importantly, the reference sample (Bi<sub>2</sub>O<sub>3</sub> NP) prepared by calcination of the self-standing Bi@BiO<sub>x</sub> NP results in the formation of several large aggregates of the nanoparticles, confirming the stabilizing role of GO, which prevents coalescence of the NP. Figure 3 shows the comparison between the HAADF-STEM images of the self-standing Bi@BiO<sub>x</sub> NP as prepared and postcalcination (Figure 3, parts a and b, respectively) with the ones stabilized by supporting them on

GO, namely GO/Bi@BiO<sub>x</sub> and GO/Bi<sub>2</sub>O<sub>3</sub> (Figure 3, parts c and d, respectively).

The nanoscale transmission electron microscopy results are in excellent agreement with large-scale X-ray diffraction (XRD) and Raman analysis. In the XRD (Figure 4), the metallic Bi phase is the only one observed for Bi@BiO<sub>x</sub> and GO/Bi@BiO<sub>x</sub>, indexed to the rhombohedral Bi (JCPDS No. 05-0519), while no relevant Bi<sub>2</sub>O<sub>3</sub> could be detected, corroborating the amorphous nature of the BiO<sub>x</sub> shell.<sup>25,27</sup> After the calcination treatment, the Bi(0) core mostly crystallizes forming the β phase of Bi<sub>2</sub>O<sub>3</sub> (tetragonal) readily indexed to the *P*42<sub>1</sub>*c* space group (ICDD crystallographic card number 01-077-5341),<sup>28</sup> while the reflections of Bi(0) have considerably decreased following such an oxidation. It is worth noting that calcination also causes a broadening of the reflection at ~27°, typical of graphitic carbon, suggesting that a reduction in the number of stacked layers of the multilayer GO has occurred.<sup>29</sup> In contrast, the thermal treatment under reducing conditions (rGO/Bi@Bi<sub>2</sub>O<sub>3</sub>) serves to crystallize the BiO<sub>x</sub> shell, while the core preserves its metallic nature, as observed by the coexistence of the reflections assigned to rhombohedral Bi and β-Bi<sub>2</sub>O<sub>3</sub> in the XRD. Additionally, micro-Raman analysis confirms the XRD results. The spectrum of the as-prepared Bi@BiO<sub>x</sub> nanoparticles confirms the presence of the two peaks (respectively at 85 and 105 cm<sup>−1</sup>) which can be assigned to the E<sub>g</sub> and A<sub>1g</sub> vibrational modes of Bi–Bi in metallic bismuth, with the frequencies having been slightly blue-shifted with respect to bulk Bi due to the decrease of particle size to the nanoscale.<sup>30</sup>

A less intense peak at 605 cm<sup>−1</sup> is also observed, attributed to the amorphous BiO<sub>x</sub> phase, perhaps being carbonated following glucose binding,<sup>31</sup> and confirming that the BiO<sub>x</sub> shell in the noncalcined samples is not crystalline.<sup>32</sup> The origin of a third well-defined peak at 293 cm<sup>−1</sup> is not clearly assigned based on literature studies; we hypothesize it is due to some specific Bi–O Raman mode of the amorphous oxide shell still covered by carbonaceous species deriving from glucose. Accordingly, a first remarkable difference after combination with GO is that such a peak is broader and significantly blue-shifted (308 cm<sup>−1</sup>), and the same occurs to the BiO<sub>x</sub> peak that is blue-shifted to 627 cm<sup>−1</sup>. No signal pattern assignable to specific Bi<sub>2</sub>O<sub>3</sub> phases is observed, indicating the amorphous nature of the Bi oxide. We interpret this result as an effect of the electronic interaction between GO and the amorphous BiO<sub>x</sub> shell, in agreement with the X-ray photoelectron spectroscopy (XPS) discussed later on. As anticipated on the basis of XRD, the crystallization of the Bi oxide in GO/Bi<sub>2</sub>O<sub>3</sub> is verified by the appearance of three new peaks at ca. 123, 315, and 465 cm<sup>−1</sup> attributed to Bi–O stretching modes in β-Bi<sub>2</sub>O<sub>3</sub>.<sup>31,33–35</sup> Meanwhile, the signature of GO in both GO/Bi@BiO<sub>x</sub> and GO/Bi<sub>2</sub>O<sub>3</sub> is clearly visible, with the D and G bands appearing at 1350 and 1570 cm<sup>−1</sup> respectively, the former related to the A<sub>1g</sub> breathing mode and the latter, together with another band (2D band) at 2700 cm<sup>−1</sup>, associated with the first- and second-order allowed Raman mode E<sub>2g</sub>.<sup>36</sup> It is worth noting that both the low D/G bands intensity ratio and the sharpness and intensity of the 2D band indicate that the starting GO has a low level of oxidation and a small disorder, while the calcination treatment induces creation of defects, presumably by insertion of additional oxygen functionalities.<sup>37</sup> In order to avoid any artifact in the interpretation of the signal shift, we also ran a 80-point micro-Raman mapping of a selected area of the GO/Bi@BiO<sub>x</sub> sample. In such a specific region, the vast majority of the

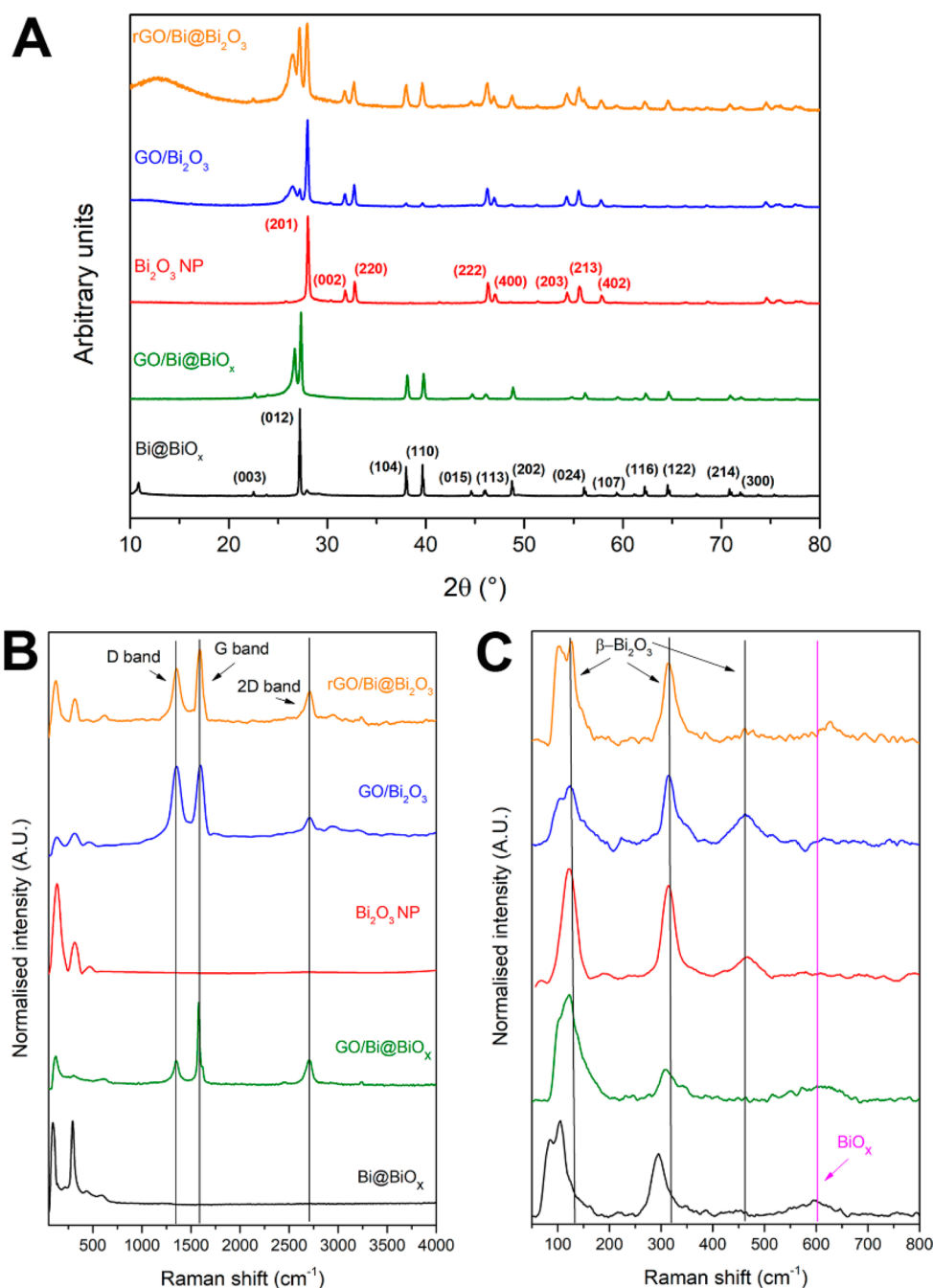


**Figure 4.** XRD and Raman analysis. (A) Powder XRD patterns of GO,  $\text{Bi}_2\text{O}_3$  NP,  $\text{Bi@BiO}_x$ , and of all three nanocomposites with crystal reflections identified and indexed to either rhombohedral Bi or  $\beta\text{-Bi}_2\text{O}_3$ ; (B) full range Raman spectra of GO,  $\text{Bi}_2\text{O}_3$  NP,  $\text{Bi@BiO}_x$ , and of all three nanocomposites showing also the D, G, and 2D bands relative to GO; (C) Raman in the range 0–800  $\text{cm}^{-1}$  showing the bands relative to  $\beta\text{-Bi}_2\text{O}_3$  and amorphous  $\text{BiO}_x$ .

material is the composite ( $\text{GO/Bi@BiO}_x$ ), but there is also a small fraction of stand-alone  $\text{Bi@BiO}_x$ . The analysis of the spectra confirms that the Raman patterns are different depending on whether the laser is focusing on the nanocomposite or on the isolated  $\text{Bi@BiO}_x$  NPs, in particular with the peak at  $306\text{ cm}^{-1}$  being shifted when coupled with GO ( $315\text{ cm}^{-1}$ ). Moreover, the peak due to amorphous  $\text{BiO}_x$  is barely visible in the stand-alone  $\text{Bi@BiO}_x$  and centered at  $607\text{ cm}^{-1}$ , while is better defined and centered at  $627\text{ cm}^{-1}$  in the nanocomposite (Figure S7). Analysis of  $\text{rGO/Bi@Bi}_2\text{O}_3$  indicates that the reduction treatment has a beneficial effect in partially restoring a smaller level of defects, as expected for

reduced GO and indicated by the decrease of the D band intensity in relation to the G band.<sup>38</sup> Moreover, the  $\beta$  phase pattern is also found, together with a peak  $103\text{ cm}^{-1}$  characteristic of metallic Bi.

X-ray photoelectron spectroscopy (XPS) provides the superficial electronic states of the elements so that it gives a detailed understanding on the interface GO/Bi oxide. XPS confirmed the presence of C and Bi elements in the analyzed samples (Figure 5). The high-resolution XPS of the Bi 4f core level of all the five samples shows the signature doublet of Bi with binding energies (BE) at 159.2 and 164.5 eV associated with the  $\text{Bi}^{5+} 4f_{7/2}$  and  $\text{Bi}^{5+} 4f_{5/2}$ ,<sup>39</sup> although interesting

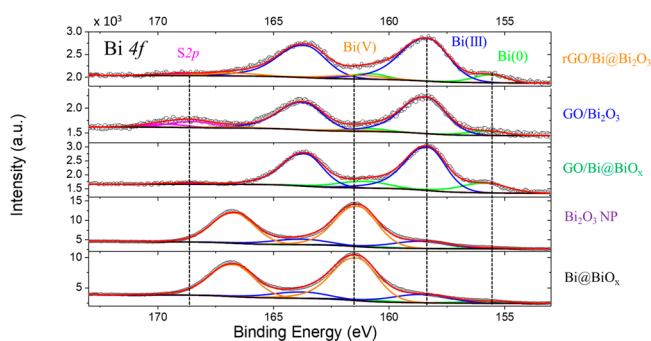


**Figure 5.** XPS analysis. High-resolution XPS spectra in the Bi 4f region. Colors of the captions are associated with the materials as follows: black (Bi@BiO<sub>x</sub>), green (GO/Bi@BiO<sub>x</sub>), blue (GO/Bi<sub>2</sub>O<sub>3</sub>), orange (rGO/Bi@Bi<sub>2</sub>O<sub>3</sub>), and purple (Bi<sub>2</sub>O<sub>3</sub> NP).

differences are observed among the samples. In the as-prepared Bi@BiO<sub>x</sub> NP and in the calcined Bi<sub>2</sub>O<sub>3</sub> NP, the BE of the two main peaks is located at 161.3 eV (orange components of Figure 5) plus its spin-orbit coupling peak at 166.6 eV, in agreement with an oxidation number of the metal of 5+.<sup>40</sup> The additional presence of two small contributions with BE of 155.5 and 158.4 eV are associated with metallic Bi (Figure 5A, green line)<sup>41,42</sup> and Bi<sup>3+</sup>.<sup>43–45</sup> The overall Bi 4f picture is consistent with the small penetration range of XPS, which makes difficult to detect the internal Bi core, while the oxidized shell is readily observed. The fact that the outer shell of the Bi oxide is overoxidized suggests a tendency of the NPs to react with atmosphere. However, once the Bi@BiO<sub>x</sub> NP are combined with GO (GO/Bi@BiO<sub>x</sub>), the doublet is shifted toward lower BE (158.3 and 163.65 eV) confirming, as hypothesized after Raman analysis, that there is an electronic interaction between the GO and Bi@BiO<sub>x</sub> (Figure 5, green line). Calcination of the composite (GO/Bi<sub>2</sub>O<sub>3</sub>) does not alter such a BE shift, implying that even in the crystallized form, the Bi<sub>2</sub>O<sub>3</sub> is still electronically interacting with GO. The metallic Bi components is still quite visible in the rGO/Bi@Bi<sub>2</sub>O<sub>3</sub> sample, confirming that the thermal treatment under reductive conditions preserves the metallic Bi, while in the calcined sample, this contribution is very low, in agreement with XRD where the contribution of the Bi(0) is very low. This suggests that GO may contribute to the donation of electron density on the outer Bi atoms constituting the core, favoring their reduction. It is worth stressing that the Bi(0) components change as a function of the different treatment of the samples: the trend of this variation is reported in Table 1. In the Bi 4f region is possible to see a small component at 168.5 eV arising from sulfur impurity. C 1s peaks of GO/Bi@BiO<sub>x</sub> were deconvoluted into four components at 284.0, 285.3, 287.2, and 290.0 eV, plus a shakeup component centered at 293.9 eV, which are ascribed to the sp<sup>2</sup>/sp<sup>3</sup> carbons, C–OH/C–O–C, C=O bond, and O=C=O respectively, arising from the

**Table 1.** Semi-Quantitative XPS Relative to the % of Bi(0), Bi(III), and Bi(IV) All over the Total Amount of Bismuth

sample	% Bi(0)	% Bi(III)	% Bi(V)
rGO/Bi@Bi <sub>2</sub> O <sub>3</sub>	12.0	81.0	7.0
GO/Bi <sub>2</sub> O <sub>3</sub>	8.0	86.0	6.0
GO/Bi@BiO <sub>x</sub>	20.0	78.0	2.0
Bi@BiO <sub>x</sub> -F	4.0	19.0	77.0
Bi@BiO <sub>x</sub> -C	3.0	19.0	78.0

functional groups of GO (Figure S9).<sup>46–48</sup> Consistently, in the nanocomposites prior to and after the thermal treatments, the relative intensities of such peaks are changed, as the treatments remove most of the GO oxygenated functional groups. The overall picture indicates that the electronic states of the Bi oxide phase are altered by the presence of GO,<sup>49</sup> which does not act as a mere inert support for the nanoparticles.

**CO<sub>2</sub>RR Electrocatalytic Performance.** The CO<sub>2</sub>RR catalytic activity was evaluated as a function of applied potential, carried out by performing chronoamperometry (CA) experiments in CO<sub>2</sub>-saturated KHCO<sub>3</sub> for 1 h and 50 min (ranging from −0.4 to −0.9 V vs RHE). Both gas-phase and liquid phase were quantified (the former via gas chromatography, GC, and the latter by ionic chromatography, IC, see the Supporting Information) after the CA in order to determine the product selectivity, reported as the Faraday efficiency (FE). Figure 6 shows, in addition to the FE values, the average values of the involved current density (*j*) during the CA. All the nanocomposites (GO/Bi@BiO<sub>x</sub>, GO/Bi<sub>2</sub>O<sub>3</sub> and rGO/Bi@Bi<sub>2</sub>O<sub>3</sub>) exhibit good catalytic activity for CO<sub>2</sub>RR with HCOOH as the dominant product, with the formation of HCOOH attained at potentials very near the thermodynamic potential.<sup>50</sup> In all cases, also hydrogen evolution reaction (HER) occurs to different extents depending on the catalyst and the applied potential. The nanocomposites are also compared with the CO<sub>2</sub>RR electrocatalytic performance by GO-free Bi<sub>2</sub>O<sub>3</sub>. Control experiments show that HCOOH production is completely suppressed in the absence of CO<sub>2</sub>, while any possible contribution in the HCOOH production from the nanomaterial is excluded on the basis of the comparison of the CO<sub>2</sub>RR activity with the GO (Figure S10). For all the nanocomposites the presence of GO significantly increases the current density for CO<sub>2</sub>RR and the FE<sub>HCOOH</sub> (Figure 6) while, importantly, the onset potential is set at earlier values (Figure 9). As we previously reported in the case of HER by oxidized carbon nanotubes/titanium oxide nanocomposites, the carbon-metal oxide turns out less electrocatalytically active in the as prepared nanocomposites. In fact, in the fresh materials, the metal oxide is still in an amorphous state and the CNS presents too many COOH functional groups, leading to a less efficient electronic communication.<sup>51</sup> This is also observed here in the case of the as prepared GO/Bi@BiO<sub>x</sub> nanocomposite as compared to the two thermally treated catalysts.

In addition, the difference in the hierarchical structures is reflected in significantly different catalytic behavior. The FE<sub>HCOOH</sub> for rGO/Bi@Bi<sub>2</sub>O<sub>3</sub> reaches a maximum value of 38% at −0.5 V vs RHE (corresponding to a HCOOH production rate of 3 ppm h<sup>−1</sup>), with a very small overpotential (100 mV), and declines with decreasing the applied potential, while H<sub>2</sub> is always formed in relatively high FE throughout the explored potential range (part A). In contrast, GO/Bi<sub>2</sub>O<sub>3</sub> is able to form HCOOH with a higher absolute FE in the more negative range (−0.7 to −0.9 V) peaking at −0.8 V (46%), with an HCOOH production rate of 73 ppm h<sup>−1</sup>, while the FE for the HER process is relatively small. Nevertheless, the FE<sub>HCOOH</sub> at −0.5 V is much lower (11%) in comparison with that of rGO/Bi@Bi<sub>2</sub>O<sub>3</sub>. From these results, we can conclude that the metallic Bi core plays a critical role in anticipating the potential for HCOOH formation, albeit the fact that Bi<sub>2</sub>O<sub>3</sub> is only present in the shell of the NP may be the cause for the modest current density, whereas in GO/Bi<sub>2</sub>O<sub>3</sub> the amount of the Bi oxide is comparatively larger (NPs are fully oxidized).

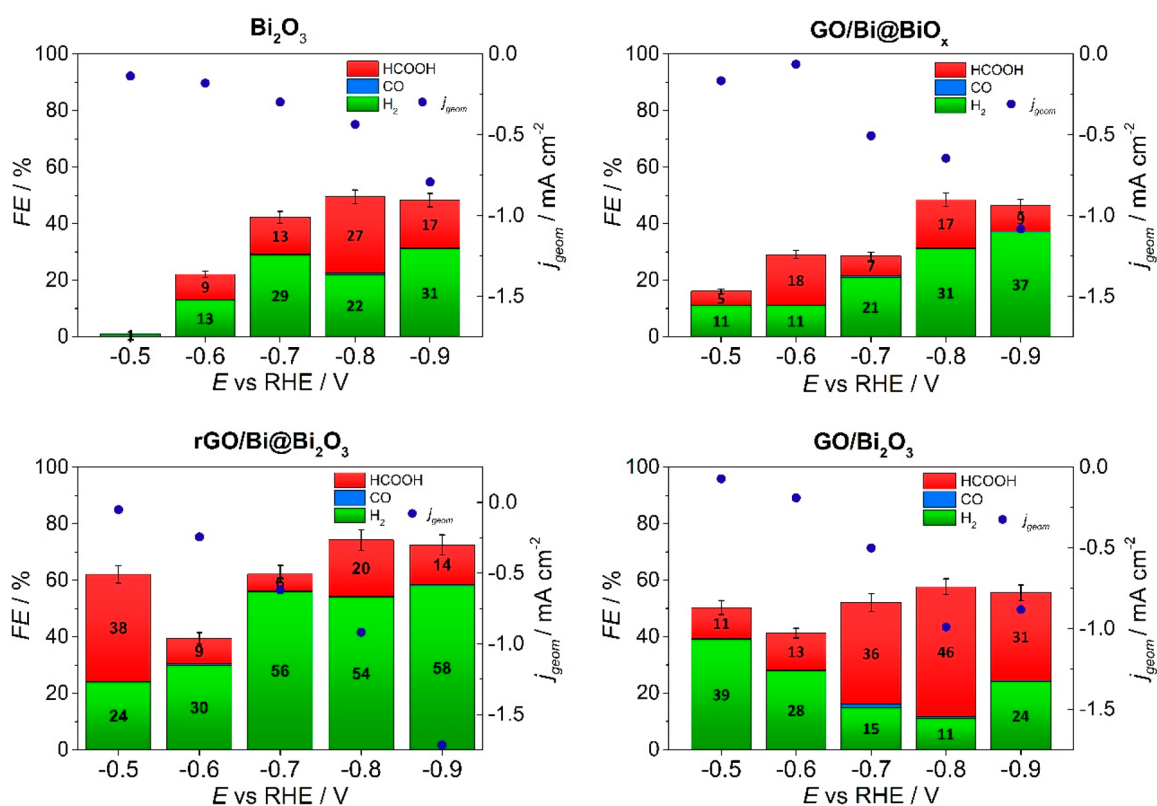


**Figure 6.** CO<sub>2</sub>RR performance. Faradaic efficiency (FE) of detectable CO<sub>2</sub>RR products in CO<sub>2</sub>-saturated KHCO<sub>3</sub> 0.5 M (pH 7.5): H<sub>2</sub> (green), CO (light blue) and HCOOH (red) for (a) Bi<sub>2</sub>O<sub>3</sub>, (b) GO/Bi@BiO<sub>x</sub>, (c) rGO/Bi@Bi<sub>2</sub>O<sub>3</sub>, and (d) GO/Bi<sub>2</sub>O<sub>3</sub>. The blue points indicate the mean current density of sample at that potential; the values are shown on the right axis.

This is in line with previous observations during CO<sub>2</sub>RR by Bi<sub>2</sub>O<sub>3</sub> catalysts that upon reduction to metallic Bi could generate higher HCOOH current densities.<sup>31</sup> As we previously reported in the case of HER catalyzed by oxidized carbon nanotubes/titanium oxide nanocomposites, the carbon–metal oxide turns out to be less electrocatalytically active in the as prepared nanocomposites. In fact, in the fresh materials, the metal oxide is still in an amorphous state and the CNS presents too many COOH functional groups, leading to a less efficient electronic communication.<sup>51</sup> This is also observed here in the case of the as prepared GO/Bi@BiO<sub>x</sub> nanocomposite as compared to the two thermally treated catalysts, which show in general lower FE<sub>HCOOH</sub> at any potential. The criticality of the CNS-MO intimate contact is also demonstrated by measuring the performances of the electrocatalyst made by physically mixing GO with Bi<sub>2</sub>O<sub>3</sub> (Figure S11), which gave similar current density to those of GO/Bi<sub>2</sub>O<sub>3</sub> but much worse electrocatalytic activities and lower stability than GO/Bi<sub>2</sub>O<sub>3</sub>. This result demonstrated not only that GO is instrumental to simply enhance the total current density by an overall improved conductivity (capacitive current) but also it contributes to an improved electron mobility toward the active Bi oxide sites, thus boosting the electrocatalytic performance.

The formic acid production rate plot (Figure 7) notes the difference in the potential range for CO<sub>2</sub>RR selectivity: the HCOOH production is higher for rGO/Bi@Bi<sub>2</sub>O<sub>3</sub> until −0.6 V, while GO/Bi<sub>2</sub>O<sub>3</sub> becomes more active in the range −0.7 to −0.9 V. However, it is worth noting that, in terms of productivity, GO/Bi<sub>2</sub>O<sub>3</sub> reaches a peak at −0.8 V and then there is a decline, whereas for rGO/Bi@Bi<sub>2</sub>O<sub>3</sub> the HCOOH

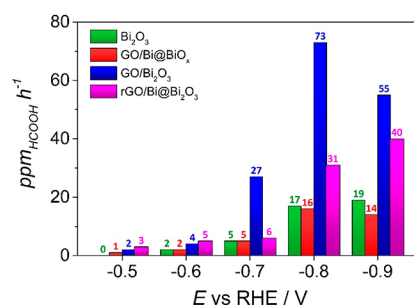


**Figure 7.** HCOOH productivity by the different catalysts. Formic acid production rate in ppm h<sup>-1</sup> at different potentials for Bi<sub>2</sub>O<sub>3</sub> (green), GO/Bi@BiO<sub>x</sub> (red), rGO/Bi@Bi<sub>2</sub>O<sub>3</sub> (pink), and GO/Bi<sub>2</sub>O<sub>3</sub> (blue).

productivity increases linearly with moving toward more negative potential, despite the drop in selectivity. This is a result of the much higher current density achieved when using the rGO, and we presume that also the Bi metal core contributes to a better electron transfer toward the Bi<sub>2</sub>O<sub>3</sub> active phase (see below). A comparison of HCOOH productivity with the free-standing bulk Bi<sub>2</sub>O<sub>3</sub> indicates that the thermally treated nanocomposites are considerably more efficient at any explored potential, with maximum productivity by GO/Bi<sub>2</sub>O<sub>3</sub> at −0.8 V being 4 times higher than bulk Bi<sub>2</sub>O<sub>3</sub>. Importantly, nanocomposites also displayed great chemical and mechanical stability with a constant FE% in prolonged electrosynthesis (>18 h, at −0.8 V; see Figure S12).

The electrochemical peculiar features of Bi<sub>2</sub>O<sub>3</sub> and the role of GO as well as of the metallic Bi in relation to CO<sub>2</sub> activation were investigated by cyclic voltammetry (CV) using a three-

electrode electrochemical cell.<sup>52</sup> The electrochemical features of bulk Bi<sub>2</sub>O<sub>3</sub> prepared by conventional synthesis was first studied. Figure 8 reports the CV of bulk Bi<sub>2</sub>O<sub>3</sub> at 20 mV s<sup>-1</sup> in Ar-saturated KOH 0.1 M.

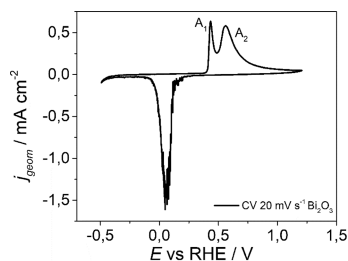
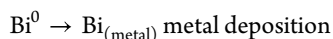
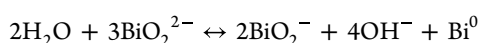
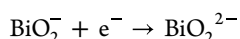
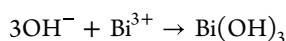
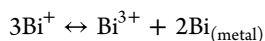
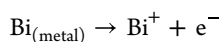


**Figure 8.** Cyclic voltammetry investigation. CV at 20 mV s<sup>-1</sup> in Ar-saturated KOH 0.1 M of Bi<sub>2</sub>O<sub>3</sub>. Two peaks are distinct for the oxidation reaction: A<sub>1</sub> is the oxidation of Bi metal sites presents in the porosity of nanoparticles, while the A<sub>2</sub> peak is due to oxidation of Bi metal sites on nanoparticles surface. The potentials were corrected post measurement for the ohmic drop, considering the resistance of system.

Under an open circuit potential condition, the material is completely oxidized ( $E_{oc} = 0.89$  V vs RHE). The bismuth oxide in contact with the alkaline solution undergoes a partial dissolution into the ionic species BiO<sub>2</sub><sup>2-</sup>.<sup>52</sup> The cathodic peak is due in the main to reduction of dissolved species BiO<sub>2</sub><sup>2-</sup>, according to these reactions.<sup>53</sup>



The oxidation peak A<sub>2</sub> and the subsequent plateau are due to the oxidation of Bi metal to Bi(III). While the peak A<sub>1</sub> is explained by Vivier et al. as the oxidation of small fraction of Bi metal sites to Bi(III) in the microporous cavities, where the amount of reactant is limited, the oxidation happens until exhaustion of OH<sup>-</sup> species. In both cases, the electrochemical reactions follow these reaction mechanisms:<sup>53</sup>



When no potential is applied, the Bi(OH)<sub>3</sub> and BiOOH evolve spontaneously to form Bi<sub>2</sub>O<sub>3</sub>. The CV of both composite GO/Bi<sub>2</sub>O<sub>3</sub> and rGO/Bi@Bi<sub>2</sub>O<sub>3</sub> were then compared with that of bulk Bi<sub>2</sub>O<sub>3</sub> to gain insights into the role of the CNS as well as of the metallic Bi. As a first important observation, the Bi<sub>2</sub>O<sub>3</sub> has a lower current than samples with carbon support, and as expected, the capacitance of the double layer is 100 times higher for both composites (Figure 9 and Figure S13). Interestingly, the Faradaic current for GO/Bi<sub>2</sub>O<sub>3</sub> and rGO/Bi@Bi<sub>2</sub>O<sub>3</sub> is approximately three times higher as compared with that of Bi<sub>2</sub>O<sub>3</sub>. Based on our previous endeavors on CO<sub>2</sub>RR catalyzed by CNS–metal oxide nanohybrids,<sup>18,19</sup> we are confident in relating this effect to higher electrical conductivity of the GO, which reduces the

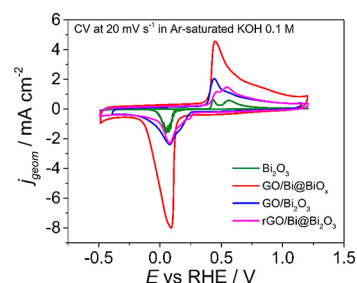


**Figure 9.** Cyclic voltammetry investigation. Cyclic voltammograms at 20 mV s<sup>-1</sup> in Ar-saturated KOH 0.1 M of Bi<sub>2</sub>O<sub>3</sub> (green), GO/Bi@Bi<sub>2</sub>O<sub>3</sub> (red), GO/Bi<sub>2</sub>O<sub>3</sub> (blue), and rGO/Bi@Bi<sub>2</sub>O<sub>3</sub> (pink). The potentials were corrected post measurement for the ohmic drop, considering the resistance of the system.

internal system resistance and supplies electrons to the metal oxide, activating the Bi<sub>2</sub>O<sub>3</sub> nanoparticles on support. In contrast, the resistance and aggregation of pure Bi<sub>2</sub>O<sub>3</sub> can decrease the electrochemical active surface area.

The CNS support also increases the stability of the Bi<sub>2</sub>O<sub>3</sub> nanoparticles. In fact, for a sample with pure Bi<sub>2</sub>O<sub>3</sub>, the faradaic current decreases with the increase in the number of cycles. It is possible to notice the different CV patterns between GO/Bi<sub>2</sub>O<sub>3</sub> and rGO/Bi@Bi<sub>2</sub>O<sub>3</sub>, where in the first case the A<sub>1</sub> peak is larger than A<sub>2</sub>, while for the sample with rGO, the A<sub>1</sub> peak decreases in favor of the A<sub>2</sub> peak. This observation well fits with the different structures of the two nanocomposites, whereby the metallic Bi core in the rGO/Bi@Bi<sub>2</sub>O<sub>3</sub>, and this particular core–shell motif plays a role in determining the electrochemical behavior. To this end, it is worth reporting previous findings with other core–shell electrocatalysts, such as Cu@SnO<sub>2</sub>, which exhibited variable selectivity depending on the thickness of the oxide layer, with theoretical calculations indicating that possible alloying of the SnO<sub>2</sub> with Cu and resulting synergy, causing a compression of the oxide shell to trigger CO or HCOOH depending on the shell thickness.<sup>54</sup> We finally performed a compositional optimization study of the GO/Bi<sub>2</sub>O<sub>3</sub> to further boost HCOOH production rates. For this purpose, two additional samples were investigated, with a higher (GO/Bi<sub>2</sub>O<sub>3</sub> 3:1) or lower Bi<sub>2</sub>O<sub>3</sub> loadings (GO/Bi<sub>2</sub>O<sub>3</sub> 5:1), respectively. Interestingly, although the current densities do not change among the three catalysts, the FE is not directly proportional to the amount of Bi<sub>2</sub>O<sub>3</sub> present in the sample. In fact, the GO/Bi<sub>2</sub>O<sub>3</sub> 4:1 catalyst shows the best performance for CO<sub>2</sub>RR, with FE<sub>HCOOH</sub> as high as 46% at -0.8 V, where the normalized formic acid production rate is 484 ppm<sub>HCOOH</sub> h<sup>-1</sup> g<sub>Bi2O3</sub><sup>-1</sup>. Instead, with GO@Bi<sub>2</sub>O<sub>3</sub> 3:1, bearing a higher amount of Bi<sub>2</sub>O<sub>3</sub>, FE<sub>HCOOH</sub> never exceed 10% until -0.8 V, with an increment at -0.9 V (Figure S14). It can therefore be deduced that nonoptimized GO/Bi<sub>2</sub>O<sub>3</sub> may favor the reduction of CO<sub>2</sub> to formic acid upon a fine balancing between the number of active sites and the material resistance (higher, e.g., in GO@Bi<sub>2</sub>O<sub>3</sub> 3:1 because of the relative lower amount of conductive GO). In line with it, GO@Bi<sub>2</sub>O<sub>3</sub> 5:1 shows significantly poorer CO<sub>2</sub>RR performances, where the top FE<sub>HCOOH</sub> is a mere 8% (at -0.9 V) and a greater selectivity for the HER process is instead observed, evidently deriving from the overriding HER activity of the GO, therein present in much larger relative amounts (Figure S14). It must be noted that, in all catalytic experiments, the intrinsic FE(HCOOH) of the Bi oxide active phase may be underestimated as at potentials more negative

than  $-0.7$  V, and there is also a contribution to HER by the graphene support, which cannot be avoided, as evaluated by screening the HER activity in  $\text{CO}_2$  by rGO at various potentials (Figure S15). Table S1 presents a comparison with other Bi-base electrocatalysts derived however from more complex synthetic procedures and under different electrochemical cell conditions.

## CONCLUSIONS

In conclusion, we carried out an in depth analysis on the role of GO when integrated with  $\text{Bi}_2\text{O}_3$  nanoparticles in the electrocatalytic reduction of  $\text{CO}_2$ , revealing remarkable differences depending on the structures. The presence of GO in intimate contact with the active phase ( $\text{Bi}_2\text{O}_3$ ) causes a remarkable increase in the  $\text{CO}_2\text{RR}$  performance toward the synthesis of formic acid. The results herein reinforce the concept that interfaces of MO with CNS promotes the activity and selectivity of the MO catalysts, offering an avenue to increase the electron trafficking nearby the MO, and contributing in a significant fashion to the long-term stability of the nanostructured catalysts. Differences were noted depending on the degree of oxidation of the carbon scaffold, with the rGO being more effective in favoring electron mobility as compared with the GO, thus facilitating electron transfers. Moreover, we prove that the adjustment of the hierarchy of the nanocomposite, by maintaining the metallic Bi(0) native core, gives rise to the formation of a double interfacial effect by the rGO and Bi(0) on the active  $\text{Bi}_2\text{O}_3$  shell, resulting in a dramatic change of the catalytic behavior, such as an anticipation in the onset potential for  $\text{CO}_2\text{RR}$  with concomitant higher  $\text{FE}_{\text{HCOOH}}$  at near-thermodynamic potential. The study lays fundamental aspects in the development of CNS/MO based electrocatalysts, although the absolute performance is yet to be optimized by adjusting the synthetic strategies and by increasing the mass transport (e.g., use of gas diffusion electrodes). In particular, the first aim will have to be to decrease the  $\text{Bi}@\text{Bi}_2\text{O}_3$  particle size in order to (i) enhance the electroactive mass activity and (ii) enhance the carbon-metal oxide interface contact area. Further integration, within the nanocomposite, of a third metal phase could lead to coupled  $\text{CO}_2\text{RR}$  mechanism in order to attempt the synthesis of more challenging ( $\text{C}_{2+}$ ) carboxylic acids.

## ASSOCIATED CONTENT

### Supporting Information

The Supporting Information is available free of charge at <https://pubs.acs.org/doi/10.1021/acsaem.2c02013>.

TEM analysis,  $\text{CO}_2\text{RR}$  catalytic performance differences between GO vs  $\text{GO}/\text{Bi}_2\text{O}_3$ , effect of the GO-MO interface on  $\text{CO}_2\text{RR}$  performance, stability, capacitance of double layer of  $\text{Bi}_2\text{O}_3$  and  $\text{rGO}/\text{Bi}@\text{Bi}_2\text{O}_3$ , the effect of  $\text{Bi}_2\text{O}_3$  loading on  $\text{CO}_2\text{RR}$  and rGO  $\text{CO}_2\text{RR}$  performances (PDF)

## AUTHOR INFORMATION

### Corresponding Authors

Michele Melchionna – Department of Chemical and Pharmaceutical Sciences, University of Trieste and Consortium INSTM, 34127 Trieste, Italy; [orcid.org/0000-0001-9813-9753](https://orcid.org/0000-0001-9813-9753); Email: [melchionnam@units.it](mailto:melchionnam@units.it)

Giovanni Valenti – Department of Chemistry “Giacomo Ciamician”, University of Bologna and Consortium INSTM,

40126 Bologna, Italy; [orcid.org/0000-0002-6223-2072](https://orcid.org/0000-0002-6223-2072);

Email: [g.valenti@unibo.it](mailto:g.valenti@unibo.it)

Paolo Fornasiero – Department of Chemical and Pharmaceutical Sciences, University of Trieste and Consortium INSTM, 34127 Trieste, Italy; ICCOM-CNR, University of Trieste, 34127 Trieste, Italy; [orcid.org/0000-0003-1082-9157](https://orcid.org/0000-0003-1082-9157); Email: [pfornasiero@units.it](mailto:pfornasiero@units.it)

## Authors

Miriam Moro – Department of Chemistry “Giacomo Ciamician”, University of Bologna and Consortium INSTM, 40126 Bologna, Italy

Simone Adorinni – Department of Chemical and Pharmaceutical Sciences, University of Trieste and Consortium INSTM, 34127 Trieste, Italy

Lucia Nasi – CNR-IMEM Institute, 43124 Parma, Italy

Sara Colussi – Department Politecnico, University of Udine, Unità di Ricerca INSTM Udine, 33100 Udine, Italy; [orcid.org/0000-0001-5316-1746](https://orcid.org/0000-0001-5316-1746)

Lorenzo Poggini – Institute of Chemistry of Organometallic Compounds, National Research Council of Italy (ICCOM-CNR), 50019 Sesto Fiorentino, Florence, Italy

Silvia Marchesan – Department of Chemical and Pharmaceutical Sciences, University of Trieste and Consortium INSTM, 34127 Trieste, Italy

Francesco Paolucci – Department of Chemistry “Giacomo Ciamician”, University of Bologna and Consortium INSTM, 40126 Bologna, Italy; [orcid.org/0000-0003-4614-8740](https://orcid.org/0000-0003-4614-8740)

Maurizio Prato – Department of Chemical and Pharmaceutical Sciences, University of Trieste and Consortium INSTM, 34127 Trieste, Italy; Carbon Nanobiotechnology Laboratory, CIC biomaGUNE, 20009 Donostia-San Sebastian, Spain; Ikerbasque, Basque Foundation for Science, 48013 Bilbao, Spain; [orcid.org/0000-0002-8869-8612](https://orcid.org/0000-0002-8869-8612)

Complete contact information is available at: <https://pubs.acs.org/doi/10.1021/acsaem.2c02013>

## Author Contributions

The manuscript was written through contributions of all authors. All authors have given approval to the final version of the manuscript.

## Notes

The authors declare no competing financial interest.

## ACKNOWLEDGMENTS

This work was supported by the University of Trieste, INSTM, the European Commission (H2020 - RIA-CE-NMBP-25 Program, Grant No. 862030). M.Me. kindly acknowledges the FRA2022, funded by the University of Trieste. G.V. and M.P. acknowledge the Italian Ministry of Education MIUR (cofin Prot. 2017PBXPN4). The authors thank Dr. Enrico Verlatto from CNR of Padua for the IC analysis. We also thank B. Cortigiani for his assistance in using the CeTeCS platform and acknowledge “progetto Dipartimenti di Eccellenza 2018-2022 (ref. no. B96C1700020008)” and Fondazione Ente Cassa di Risparmio di Firenze for financial support.

## REFERENCES

(1) Garg, S.; Li, M.; Weber, A. Z.; Ge, L.; Li, L.; Rudolph, V.; Wang, G.; Rufford, T. E. Advances and challenges in electrochemical  $\text{CO}_2$  reduction processes: an engineering and design perspective looking

beyond new catalyst materials. *J. Mater. Chem. A* **2020**, *8* (4), 1511–1544.

(2) Appel, A. M.; Bercaw, J. E.; Bocarsly, A. B.; Dobbek, H.; DuBois, D. L.; Dupuis, M.; Ferry, J. G.; Fujita, E.; Hille, R.; Kenis, P. J. A.; Kerfeld, C. A.; Morris, R. H.; Peden, C. H. F.; Portis, A. R.; Ragsdale, S. W.; Rauchfuss, T. B.; Reek, J. N. H.; Seefeldt, L. C.; Thauer, R. K.; Waldrop, G. L. Frontiers, Opportunities, and Challenges in Biochemical and Chemical Catalysis of CO<sub>2</sub> Fixation. *Chem. Rev.* **2013**, *113* (8), 6621–6658.

(3) Lu, Q.; Jiao, F. Electrochemical CO<sub>2</sub> reduction: Electrocatalyst, reaction mechanism, and process engineering. *Nano Energy* **2016**, *29*, 439–456.

(4) Seh, Z. W.; Kibsgaard, J.; Dickens, C. F.; Chorkendorff, I.; Nørskov, J. K.; Jaramillo, T. F. Combining theory and experiment in electrocatalysis: Insights into materials design. *Science* **2017**, *355* (6321), No. eaad4998.

(5) Wang, X.; Wang, Z.; García de Arquer, F. P.; Dinh, C.-T.; Ozden, A.; Li, Y. C.; Nam, D.-H.; Li, J.; Liu, Y.-S.; Wicks, J.; Chen, Z.; Chi, M.; Chen, B.; Wang, Y.; Tam, J.; Howe, J. Y.; Proppe, A.; Todorović, P.; Li, F.; Zhuang, T.-T.; Gabardo, C. M.; Kirmani, A. R.; McCallum, C.; Hung, S.-F.; Lum, Y.; Luo, M.; Min, Y.; Xu, A.; O'Brien, C. P.; Stephen, B.; Sun, B.; Ip, A. H.; Richter, L. J.; Kelley, S. O.; Sinton, D.; Sargent, E. H. Efficient electrically powered CO<sub>2</sub>-to-ethanol via suppression of deoxygenation. *Nat. Energy* **2020**, *5* (6), 478–486.

(6) Zheng, X.; De Luna, P.; García de Arquer, F. P.; Zhang, B.; Becknell, N.; Ross, M. B.; Li, Y.; Banis, M. N.; Li, Y.; Liu, M.; Voznyy, O.; Dinh, C. T.; Zhuang, T.; Stadler, P.; Cui, Y.; Du, X.; Yang, P.; Sargent, E. H. Sulfur-Modulated Tin Sites Enable Highly Selective Electrochemical Reduction of CO<sub>2</sub> to Formate. *Joule* **2017**, *1* (4), 794–805.

(7) Enthaler, S.; von Langermann, J.; Schmidt, T. Carbon dioxide and formic acid—the couple for environmental-friendly hydrogen storage? *Energy Environ. Sci.* **2010**, *3* (9), 1207–1217.

(8) Han, N.; Wang, Y.; Yang, H.; Deng, J.; Wu, J.; Li, Y.; Li, Y. Ultrathin bismuth nanosheets from in situ topotactic transformation for selective electrocatalytic CO<sub>2</sub> reduction to formate. *Nat. Commun.* **2018**, *9* (1), 1320.

(9) Zhang, X.; Sun, X.; Guo, S.-X.; Bond, A. M.; Zhang, J. Formation of lattice-dislocated bismuth nanowires on copper foam for enhanced electrocatalytic CO<sub>2</sub> reduction at low overpotential. *Energy Environ. Sci.* **2019**, *12* (4), 1334–1340.

(10) Koh, J. H.; Won, D. H.; Eom, T.; Kim, N.-K.; Jung, K. D.; Kim, H.; Hwang, Y. J.; Min, B. K. Facile CO<sub>2</sub> Electro-Reduction to Formate via Oxygen Bidentate Intermediate Stabilized by High-Index Planes of Bi Dendrite Catalyst. *ACS Catal.* **2017**, *7* (8), 5071–5077.

(11) Rudnev, A. V.; Kiran, K.; Broekmann, P. Specific Cation Adsorption: Exploring Synergistic Effects on CO<sub>2</sub> Electroreduction in Ionic Liquids. *ChemElectroChem.* **2020**, *7* (8), 1897–1903.

(12) Zhang, W.; Hu, Y.; Ma, L.; Zhu, G.; Zhao, P.; Xue, X.; Chen, R.; Yang, S.; Ma, J.; Liu, J.; Jin, Z. Liquid-phase exfoliated ultrathin Bi nanosheets: Uncovering the origins of enhanced electrocatalytic CO<sub>2</sub> reduction on two-dimensional metal nanostructure. *Nano Energy* **2018**, *53*, 808–816.

(13) Gong, Q.; Ding, P.; Xu, M.; Zhu, X.; Wang, M.; Deng, J.; Ma, Q.; Han, N.; Zhu, Y.; Lu, J.; Feng, Z.; Li, Y.; Zhou, W.; Li, Y. Structural defects on converted bismuth oxide nanotubes enable highly active electrocatalysis of carbon dioxide reduction. *Nat. Commun.* **2019**, *10* (1), 2807.

(14) Yang, F.; Elnabawy, A. O.; Schimmenti, R.; Song, P.; Wang, J.; Peng, Z.; Yao, S.; Deng, R.; Song, S.; Lin, Y.; Mavrikakis, M.; Xu, W. Bismuthene for highly efficient carbon dioxide electroreduction reaction. *Nat. Commun.* **2020**, *11* (1), 1088.

(15) Zhang, Y.; Li, F.; Zhang, X.; Williams, T.; Easton, C. D.; Bond, A. M.; Zhang, J. Electrochemical reduction of CO<sub>2</sub> on defect-rich Bi derived from Bi<sub>2</sub>S<sub>3</sub> with enhanced formate selectivity. *Journal of Materials Chemistry A* **2018**, *6* (11), 4714–4720.

(16) Zhang, Y.; Zhang, X.; Ling, Y.; Li, F.; Bond, A. M.; Zhang, J. Controllable Synthesis of Few-Layer Bismuth Subcarbonate by

Electrochemical Exfoliation for Enhanced CO<sub>2</sub> Reduction Performance. *Angew. Chem., Int. Ed.* **2018**, *57* (40), 13283–13287.

(17) Lu, P.; Gao, D.; He, H.; Wang, Q.; Liu, Z.; Dipazir, S.; Yuan, M.; Zu, W.; Zhang, G. Facile synthesis of a bismuth nanostructure with enhanced selectivity for electrochemical conversion of CO<sub>2</sub> to formate. *Nanoscale* **2019**, *11* (16), 7805–7812.

(18) Melchionna, M.; Bracamonte, M. V.; Giuliani, A.; Nasi, L.; Montini, T.; Tavagnacco, C.; Bonchio, M.; Fornasiero, P.; Prato, M. Pd@TiO<sub>2</sub>/carbon nanohorn electrocatalysts: reversible CO<sub>2</sub> hydrogenation to formic acid. *Energy Environ. Sci.* **2018**, *11* (6), 1571–1580.

(19) Valenti, G.; Melchionna, M.; Montini, T.; Boni, A.; Nasi, L.; Fonda, E.; Criado, A.; Zitolo, A.; Voci, S.; Bertoni, G.; Bonchio, M.; Fornasiero, P.; Paolucci, F.; Prato, M. Water-Mediated Electro-Hydrogenation of CO<sub>2</sub> at Near-Equilibrium Potential by Carbon Nanotubes/Cerium Dioxide Nanohybrids. *ACS Appl. Energy Mater.* **2020**, *3* (9), 8509–8518.

(20) Melchionna, M.; Fornasiero, P.; Prato, M.; Bonchio, M. Electrocatalytic CO<sub>2</sub> reduction: role of the cross-talk at nano-carbon interfaces. *Energy Environ. Sci.* **2021**, *14* (11), 5816–5833.

(21) Melchionna, M.; Bonchio, M.; Paolucci, F.; Prato, M.; Fornasiero, P. Catalysis-Material Crosstalk at Tailored Nano-Carbon Interfaces. In *Making and Exploiting Fullerenes, Graphene, and Carbon Nanotubes*; Marcaccio, M., Paolucci, F., Eds.; Springer Berlin Heidelberg: Berlin and Heidelberg, Germany, 2014; pp 139–180.

(22) Liu, S.; Lu, X. F.; Xiao, J.; Wang, X.; Lou, X. W. Bi<sub>2</sub>O<sub>3</sub> Nanosheets Grown on Multi-Channel Carbon Matrix to Catalyze Efficient CO<sub>2</sub> Electroreduction to HCOOH. *Angew. Chem., Int. Ed.* **2019**, *58* (39), 13828–13833.

(23) Deng, P.; Wang, H.; Qi, R.; Zhu, J.; Chen, S.; Yang, F.; Zhou, L.; Qi, K.; Liu, H.; Xia, B. Y. Bismuth Oxides with Enhanced Bismuth-Oxygen Structure for Efficient Electrochemical Reduction of Carbon Dioxide to Formate. *ACS Catal.* **2020**, *10* (1), 743–750.

(24) Iglesias, D.; Melle-Franco, M.; Kurbasic, M.; Melchionna, M.; Abrami, M.; Grassi, M.; Prato, M.; Marchesan, S. Oxidized Nanocarbons-Tripeptide Supramolecular Hydrogels: Shape Matters! *ACS Nano* **2018**, *12* (6), 5530–5538.

(25) Chen, M.; Li, Y.; Wang, Z.; Gao, Y.; Huang, Y.; Cao, J.; Ho, W.; Lee, S. Controllable Synthesis of Core-Shell Bi@Amorphous Bi<sub>2</sub>O<sub>3</sub> Nanospheres with Tunable Optical and Photocatalytic Activity for NO Removal. *Ind. Eng. Chem. Res.* **2017**, *56* (37), 10251–10258.

(26) Lamagni, P.; Miola, M.; Catalano, J.; Hvid, M. S.; Mamakhel, M. A. H.; Christensen, M.; Madsen, M. R.; Jeppesen, H. S.; Hu, X.-M.; Daasbjerg, K.; Skrydstrup, T.; Lock, N. Restructuring Metal-Organic Frameworks to Nanoscale Bismuth Electrocatalysts for Highly Active and Selective CO<sub>2</sub> Reduction to Formate. *Adv. Funct. Mater.* **2020**, *30* (16), 1910408.

(27) Wang, Z.; Jiang, C.; Huang, R.; Peng, H.; Tang, X. Investigation of Optical and Photocatalytic Properties of Bismuth Nanospheres Prepared by a Facile Thermolysis Method. *J. Phys. Chem. C* **2014**, *118* (2), 1155–1160.

(28) Dias, L. P.; Correia, F. C.; Ribeiro, J. M.; Tavares, C. J. Photocatalytic Bi<sub>2</sub>O<sub>3</sub>/TiO<sub>2</sub>:N Thin Films with Enhanced Surface Area and Visible Light Activity. *Coatings* **2020**, *10* (5), 445.

(29) Rao, C. N. R.; Biswas, K.; Subrahmanyam, K. S.; Govindaraj, A. Graphene, the new nanocarbon. *J. Mater. Chem.* **2009**, *19* (17), 2457–2469.

(30) Onari, S.; Miura, M.; Matsuishi, K. Raman spectroscopic studies on bismuth nanoparticles prepared by laser ablation technique. *Appl. Surf. Sci.* **2002**, *197–198*, 615–618.

(31) Dutta, A.; Zelocualtecatl Montiel, I.; Kiran, K.; Rieder, A.; Grozovski, V.; Gut, L.; Broekmann, P. A Tandem (Bi<sub>2</sub>O<sub>3</sub> → Bimet) Catalyst for Highly Efficient ec-CO<sub>2</sub> Conversion into Formate: Operando Raman Spectroscopic Evidence for a Reaction Pathway Change. *ACS Catal.* **2021**, *11* (9), 4988–5003.

(32) Depablos-Rivera, O.; Martínez, A.; Rodil, S. E. Interpretation of the Raman spectra of bismuth oxide thin films presenting different crystallographic phases. *J. Alloys Compd.* **2021**, *853*, 157245.

- (33) Kim, S.; Dong, W. J.; Gim, S.; Sohn, W.; Park, J. Y.; Yoo, C. J.; Jang, H. W.; Lee, J.-L. Shape-controlled bismuth nanoflakes as highly selective catalysts for electrochemical carbon dioxide reduction to formate. *Nano Energy* **2017**, *39*, 44–52.
- (34) Pereira, A. L. J.; Sans, J. A.; Vilaplana, R.; Gomis, O.; Manjón, F. J.; Rodríguez-Hernández, P.; Muñoz, A.; Popescu, C.; Beltrán, A. Isostructural Second-Order Phase Transition of  $\beta$ -Bi<sub>2</sub>O<sub>3</sub> at High Pressures: An Experimental and Theoretical Study. *J. Phys. Chem. C* **2014**, *118* (40), 23189–23201.
- (35) Díaz-Guerra, C.; Almodóvar, P.; Camacho-López, M.; Camacho-López, S.; Piqueras, J. Formation of  $\beta$ -Bi<sub>2</sub>O<sub>3</sub> and  $\delta$ -Bi<sub>2</sub>O<sub>3</sub> during laser irradiation of Bi films studied in-situ by spatially resolved Raman spectroscopy. *J. Alloys Compd.* **2017**, *723*, 520–526.
- (36) Claramunt, S.; Varea, A.; López-Díaz, D.; Velázquez, M. M.; Cornet, A.; Cirera, A. The Importance of Interbands on the Interpretation of the Raman Spectrum of Graphene Oxide. *J. Phys. Chem. C* **2015**, *119* (18), 10123–10129.
- (37) Martins Ferreira, E. H.; Moutinho, M. V. O.; Stavale, F.; Lucchese, M. M.; Capaz, R. B.; Achete, C. A.; Jorio, A. Evolution of the Raman spectra from single-, few-, and many-layer graphene with increasing disorder. *Phys. Rev. B* **2010**, *82* (12), 125429.
- (38) Criado, A.; Melchionna, M.; Marchesan, S.; Prato, M. The Covalent Functionalization of Graphene on Substrates. *Angew. Chem., Int. Ed.* **2015**, *54* (37), 10734–10750.
- (39) Wang, J.; Zhang, H.; Hunt, M. R. C.; Charles, A.; Tang, J.; Bretcanu, O.; Walker, D.; Hassan, K. T.; Sun, Y.; Siller, L. Synthesis and Characterisation of Reduced Graphene Oxide/Bismuth Composite for Electrodes in Electrochemical Energy Storage Devices. *ChemSusChem* **2017**, *10* (2), 363–371.
- (40) Sales, M. G.; Herweyer, L.; Opila, E.; McDonnell, S. MoS<sub>2</sub> impurities: Chemical identification and spatial resolution of bismuth impurities in geological material. *Appl. Surf. Sci.* **2020**, *508*, 145256.
- (41) Sun, J.; Zheng, W.; Lyu, S.; He, F.; Yang, B.; Li, Z.; Lei, L.; Hou, Y. Bi/Bi<sub>2</sub>O<sub>3</sub> nanoparticles supported on N-doped reduced graphene oxide for highly efficient CO<sub>2</sub> electroreduction to formate. *Chin. Chem. Lett.* **2020**, *31* (6), 1415–1421.
- (42) Hu, J.; Li, H.; Huang, C.; Liu, M.; Qiu, X. Enhanced photocatalytic activity of Bi<sub>2</sub>O<sub>3</sub> under visible light irradiation by Cu(II) clusters modification. *Appl. Catal., B* **2013**, *142–143*, 598–603.
- (43) Zhao, S.-g.; Chen, F.-y.; Hao, C.-c.; Tang, Y.-b.; Shi, W.-l. Bi<sub>2</sub>O<sub>4</sub> decorated with SnO<sub>2</sub> nanoparticles as direct Z-scheme heterojunction for enhanced degradation of tetracycline under visible light irradiation. *J. Chem. Technol. Biotechnol.* **2022**, *97* (9), 2466–2476.
- (44) Jiang, T.; Wang, K.; Guo, T.; Wu, X.; Zhang, G. Fabrication of Z-scheme MoO<sub>3</sub>/Bi<sub>2</sub>O<sub>4</sub> heterojunction photocatalyst with enhanced photocatalytic performance under visible light irradiation. *Chin. J. Catal.* **2020**, *41* (1), 161–169.
- (45) Hasan, N.; Dalayoan, D. J. C.; Lee, J.; Lee, J.; Kim, J.; Bae, J.-S.; Liu, C. Ag<sub>0</sub>/Au<sub>0</sub> nanocluster loaded Bi<sub>2</sub>O<sub>4</sub> photocatalyst for methyl orange dye photodegradation. *RSC Adv.* **2021**, *11* (43), 26607–26619.
- (46) Johra, F. T.; Lee, J.-W.; Jung, W.-G. Facile and safe graphene preparation on solution based platform. *J. Ind. Eng. Chem.* **2014**, *20* (5), 2883–2887.
- (47) Biesinger, M. C. Accessing the robustness of adventitious carbon for charge referencing (correction) purposes in XPS analysis: Insights from a multi-user facility data review. *Appl. Surf. Sci.* **2022**, *597*, 153681.
- (48) Morgan, D. J. Comments on the XPS Analysis of Carbon Materials. *C* **2021**, *7* (3), 51.
- (49) Huang, L.-W.; Jeng, H.-T.; Su, W.-B.; Chang, C.-S. Indirect interactions of metal nanoparticles through graphene. *Carbon* **2021**, *174*, 132–137.
- (50) Kortlever, R.; Shen, J.; Schouten, K. J. P.; Calle-Vallejo, F.; Koper, M. T. M. Catalysts and Reaction Pathways for the Electrochemical Reduction of Carbon Dioxide. *J. Phys. Chem. Lett.* **2015**, *6* (20), 4073–4082.
- (51) Valenti, G.; Boni, A.; Melchionna, M.; Cargnello, M.; Nasi, L.; Bertoni, G.; Gorte, R. J.; Marcaccio, M.; Rapino, S.; Bonchio, M.; Fornasiero, P.; Prato, M.; Paolucci, F. Co-axial heterostructures integrating palladium/titanium dioxide with carbon nanotubes for efficient electrocatalytic hydrogen evolution. *Nat. Commun.* **2016**, *7* (1), 13549.
- (52) Vivier, V.; Cachet-Vivier, C.; Mezaille, S.; Wu, B. L.; Cha, C. S.; Nedelec, J. Y.; Fedoroff, M.; Michel, D.; Yu, L. T. Electrochemical Study of Bi[sub 2]O[sub 3] and Bi[sub 2]O[sub 2]CO[sub 3] by Means of a Cavity Microelectrode. I. Observed Phenomena and Direct Analysis of Results. *J. Electrochem. Soc.* **2000**, *147* (11), 4252.
- (53) Vivier, V.; Régis, A.; Sagon, G.; Nedelec, J. Y.; Yu, L. T.; Cachet-Vivier, C. Cyclic voltammetry study of bismuth oxide Bi<sub>2</sub>O<sub>3</sub> powder by means of a cavity microelectrode coupled with Raman microspectrometry. *Electrochim. Acta* **2001**, *46* (6), 907–914.
- (54) Li, Q.; Fu, J.; Zhu, W.; Chen, Z.; Shen, B.; Wu, L.; Xi, Z.; Wang, T.; Lu, G.; Zhu, J.-j.; Sun, S. Tuning Sn-Catalysis for Electrochemical Reduction of CO<sub>2</sub> to CO via the Core/Shell Cu/SnO<sub>2</sub> Structure. *J. Am. Chem. Soc.* **2017**, *139* (12), 4290–4293.

## Recommended by ACS

### Borocarbonitrides As Metal-Free Electrocatalysts for the Electrochemical Reduction of CO<sub>2</sub>

Mohd Monis Ayyub and C. N. R. Rao

JULY 13, 2022  
CHEMISTRY OF MATERIALS

READ 

### Metal-Free SeBN Ternary-Doped Porous Carbon as Efficient Electrocatalysts for CO<sub>2</sub> Reduction Reaction

Wei Wang, Jiayin Yuan, et al.

AUGUST 24, 2022  
ACS APPLIED ENERGY MATERIALS

READ 

### Co-, Ni-Catalyzed Borylation of Carbon Nanofibers for Oxygen Reduction Reaction in an Anion Exchange Membrane Fuel Cell

Sumanta Kumar Das, Akhila Kumar Sahu, et al.

AUGUST 02, 2022  
ACS APPLIED ENERGY MATERIALS

READ 

### Surface-Oxygen-Rich Bi@C Nanoparticles for High-Efficiency Electroreduction of CO<sub>2</sub> to Formate

Shuang Liu, Wei Chen, et al.

NOVEMBER 01, 2022  
NANO LETTERS

READ 

Get More Suggestions >